AHMET DEMIREL[©][1], EMRE CAN ÇETIN[©][1], ALI KARAKUŞ[©][1],
MEHMET ŞAHIN ATAŞ[©][1], MEHMET YILDIRIM[©][1*]

MICROSTRUCTURAL EVOLUTION AND OXIDATION BEHAVIOR OF Fe-4Cr-6Ti FERRITIC ALLOY WITH Fe_2Ti LAVES PHASE PRECIPITATES

The microstructural properties and hardness of a model ternary Fe-4Cr-6Ti ferritic alloy aged at 800°C for 8, 16 and 24 h are investigated in detail. Fine Fe_2Ti Laves phase particles precipitate in the α-Fe (ferrite) matrix phase after solutionizing and subsequent aging treatments. The size and amount of Fe_2Ti precipitates gradually increase with increasing aging time. The magnetic measurements of the aged samples confirm the variations in the microstructural properties including the volume fraction of the constituent phases, and Ti content of the α-Fe matrix phase. The mean Vickers microhardness value also increases from 203.5 to 238.4 with increasing aging time from 8 to 24 h. In addition, the cyclic oxidation behavior of 24 h aged sample, which contains maximum amount of Fe_2Ti precipitates, is also investigated in detail. X-ray diffraction analysis reveals that scale product is α-Fe_2O_3 (hematite). Significant scale spallation and void formation is observed on the surfaces of 24 h aged Fe-4Cr-6Ti sample oxidized at 500°C.

Keywords: Ferritic alloy; Microstructure; Precipitation hardening; Laves phase; Oxidation

1. Introduction

Heat-resistant ferritic steels are widely used for structural applications at high temperatures such as thermal power plants because of their outstanding thermal conductivity, lower thermal expansion coefficient, good oxidation resistance and low material cost compared to Ni-based superalloys and austenitic steels [1-5]. However, poor creep resistance at temperatures above 600°C significantly hinders their applications [4,6-8]. Considerable research attention have been conducted in order to improve the creep resistance and service temperature of heat-resistant ferritic steels [9-13]. Previous studies demonstrated that distribution of oxides, and formation of coherent or incoherent precipitates are common approaches used for strengthening heat-resistant ferritic steels [1-5,14,15]. Although the distribution of oxide particles is highly effective process, its production cost is still a major drawback [4]. In this sense, precipitation hardening is more favorable.

The microstructure of heat-resistant ferritic steels is composed of tempered martensite matrix and carbide or carbonitride particles [15]. However, dissolution of carbides at elevated temperatures has a negative effect on mechanical properties. On the other hand, Laves phase which is a thermodynamically stable intermetallic compound with AB_2 stoichiometry and topologically closed packed structure (TCP) is believed to increase high temperature mechanical properties and creep resistance [14-17]. However, formation of Laves phase decreases the toughness and ductility of steel/alloy considerably at ambient temperatures [15,18]. Yamamoto et al. [15] reported that there is an optimum balance between room- and high temperature mechanical properties of Fe_2Nb Laves phase strengthened Fe-Cr-Nb(Ni) heat-resistant ferritic steels. Additionally, it is also presented that creep resistance of a heat-resistant ferritic steel is improved due to the formation of Fe_2Nb, Fe_2W and Fe_2Ti Laves phases [15,19]. More recently, Takata et al. [14] suggested a new carbon free austenitic heat-resistant Fe-20Cr-30Ni-2Nb alloy containing certain amount of Laves phase. They presented that this steel shows excellent long-term creep resistance.

On the other hand, the coarsening of fine precipitates in such steels/alloys at high temperatures can strongly affect the mechanical properties and creep resistance [20-24]. In this respect, Abe [20] illustrated that coarsening of fine Fe_2W Laves phase precipitates in 9Cr-1W tempered martensitic steels reduces the creep rate in the transient region. Therefore, in this study, it is aimed to investigate the microstructural evolution of Fe_2Ti Laves phase in a model Fe-4Cr-6Ti alloy. In addition, oxidation

[1] KONYA TECHNICAL UNIVERSITY, FACULTY OF ENGINEERING AND NATURAL SCIENCES, DEPARTMENT OF METALLURGICAL AND MATERIALS ENGINEERING, KONYA, TURKEY

* Corresponding author : myildirim@ktun.edu.tr

behavior of 24 h aged Fe-4Cr-6Ti sample, which contains highest amount of Fe$_2$Ti Laves phase precipitates, is also investigated in detail since oxidation resistance of structural components at high temperatures is an important service life limiting parameter [25-27].

2. Experimental Procedure

2.1. Production of the Samples

A model ternary Fe-4Cr-6Ti (at. %) ferritic alloy was prepared by arc-melting technique under Ar atmosphere in order to prevent oxidation. Ultra-high purity constituents (Fe: 99.97 wt. %, Cr: 99.2 wt. % and Ti: 99.9 wt. %) were used in the production of the alloy. The Fe-4Cr-6Ti sample was remelted at least three times in order to get highly homogenous composition. The Fe-4Cr-6Ti samples were solutionized at 1000°C for 1 hour in the single phase α-Fe (ferrite) region and then aged for 8, 16 and 24 h at 800°C in the (α-Fe+Fe$_2$Ti) two phase region followed by rapid cooling to room temperature.

2.2. Characterization

The microstructural examination of the as-cast and aged samples were conducted with Nikon Eclipse MA100 model optical microscope and Hitachi SU5000 model scanning electron microscope (SEM) in the secondary electron mode. The samples for microstructural examination were prepared by standard sample preparation techniques and were etched with a mixture of % 2 Nital and picric acid solution. Circular area equivalent method is used to determine the size of the individual precipitates [28,29]. For grain boundary precipitates, only individual precipitates were taken into calculation, the precipitates forming continuous grid at the grain boundaries were excluded. The volumetric number density is calculated utilizing the relationship

$N_V = \dfrac{N_A}{2\langle R \rangle}$ [30,31], where N_A is the areal density (number of

precipitates divided by the area of the micrograph) and $\langle R \rangle$ is the mean equivalent precipitate radius. The areal density of the grain boundary precipitates is calculated according to following equation [32]:

$$\rho(\%) = \frac{(l_1 + l_2 + l_3 + l_4 + \ldots)}{L} * 100 \tag{1}$$

where ρ is the areal fraction of grain boundary precipitates, l is the length of the grain boundary precipitates and L is the length of grain boundaries.

The chemical composition of the as-cast Fe-4Cr-6Ti sample as well as the composition of the constituent phases in the aged samples were determined by Elemental Dispersive X-ray Spectroscopy (EDS) analysis. The EDS punctual analyses were performed on the bakalite mounted-polished specimens and

silver paste was applied to the specimens in order to improve conductivity. The phase analysis of the as-cast and aged samples were conducted by X-ray Diffraction (XRD) analyses utilizing Cu-Kα radiation in a Bruker D8 model diffractometer. The solvus, solidus, liquidus and Curie temperatures of the Fe-4Cr-6Ti alloy were determined from Differential Scanning Calorimetry (DSC) measurements. DSC analysis was performed using a Setaram SETSYS 16/18 model instrument within the temperature range of 200-1450°C. The calibration of the instrument was performed using high purity standard elements including Al, Zn, Pb, Ag, Au and Ni at a wide range of temperatures. The precision of the calibration was ± 1°C. Vickers microhardness measurements were done with a Microbul 1000D model microhardness test instrument with a load of 500 g for 10 s. The mean microhardness value were the average of 8 individual indentations. The magnetic behavior of the as-cast and aged Fe-4Cr-6Ti samples were characterized by hysteresis loops with utilizing an ADE Magnetics EV/9 Vibrating Sample Magnetometer (VSM).

2.3. Cyclic Oxidation Tests

The rectangular specimens of 3×6×1 mm^3 for cyclic oxidation experiments were cut by electro discharge machining. Before cyclic oxidation tests, the specimens were manually ground with SiC emery papers (320 to 1200 grit), polished with 1 μm alumina suspension, ultrasonically cleaned in acetone and dried at room temperature. During the cyclic oxidation test, sample was first weighed using an electronic balance with an accuracy of 0.01 mg, put into an alumina crucible and then placed into the muffle furnace at 500°C. After 5 h exposure, the crucible was took out from the furnace and left to cooling. Then, the sample was reweighed. After oxidation, the oxidation products were characterized by XRD and SEM equipped with EDS detector.

3. Results and Discussion

3.1. As-cast Fe-4Cr-6Ti alloy

The EDS composition of the as-cast Fe-4Cr-6Ti alloy is given in TABLE 1. The nominal and analyzed compositions are very good agreement with each other. Any impurities are not detected since ultrahigh-purity starting materials are used. The microstructure (Fig. 1a) of the as-cast Fe-4Cr-6Ti alloy is composed of coarse and equiaxed α-Fe (ferrite) grains having an average grain diameter of 110 ± 7 μm. The XRD analysis (Fig. 1b) reveals that α-Fe (JCPDS Card No: 89-4186) is the only crystalline phase without formation of any intermetallic compound. The lattice parameter of α-Fe phase for the as-cast Fe-4Cr-6Ti alloy is calculated as 2.877 Å using XRD data. The calculated lattice parameter of α-Fe phase is slightly larger than that of the pure α-Fe (2.860 Å [33] and 2.866 Å [34]). This result implies a reasonable lattice enlargement due to atomic radii difference between Fe, Cr and Ti atoms. Although atomic

radii of Fe (r_{Fe} = 1.260 Å) is close to that of Cr (r_{Cr} = 1.256 Å), it is strongly lower than that of Ti (r_{Ti} = 1.450 Å) [35, 36]. Thus, incorporation of Ti atoms into α-Fe expands the α-Fe lattice.

Nominal and analyzed compositions
of the as-cast Fe-4Cr-6Ti sample

Nominal composition (at. %)	EDS (at. %)			EDS (wt. %)		
Fe-4Cr-6Ti	Fe	Cr	Ti	Fe	Cr	Ti
	89.43	3.98	6.60	90.53	3.75	5.72

Moreover, the room-temperature magnetic properties of the as-cast Fe-4Cr-6Ti alloy is also investigated and the representative hysteresis curve is displayed in Fig. 1(c). The as-cast Fe-4Cr-6Ti alloy exhibits soft ferromagnetic behavior with a saturation magnetization (M_s) of 191.4 emu/g. Pure α-Fe has a M_s value of 217.9 emu/g [37]. The observed M_s value of the as-cast Fe-4Cr-6Ti alloy is reasonably lower than that of pure α-Fe. The substitution of non-magnetic elements (Cr and Ti) into the α-Fe lattice decreases the saturation magnetization.

Prior to aging, thermal analysis measurements (Fig. 1(d)) is performed to determine the solutionizing and aging temperatures correctly. In this manner, solvus, solidus and other transformation temperatures (curie and liquidus) are determined from the DSC heating and cooling curves. The measured transformation temperatures are listed in TABLE 2. Moreover, the experimentally measured transformation temperatures are consistent with the Fe-Ti binary phase diagram [38-42].

Characteristic temperatures of the as-cast Fe-4Cr-6Ti sample
determined from DSC analysis

Characteristic temperatures (°C)	Curie	Solvus	Solidus	Liquidus
Heating	769	n.a.	1274	1381
Cooling	771	892	1285	1385

3.2. Aged Fe-4Cr-5Ti alloys

The microstructures of the Fe-4Cr-6Ti alloys aged at 800°C for 8, 16 and 24 h are shown in Fig. 2. The microstructures of all aged alloys are composed of polygonal α-Fe grains with homogenously distributed precipitates. These precipitates are identified as Fe_2Ti Laves phase based on the EDS (Fig. 3) analysis. The Fe_2Ti precipitates form both within the grains and along the grain boundaries. With increasing aging time, the size and amount of the Fe_2Ti precipitates inside the grains (TABLE 3) continuously increase, whereas the number density and the precipitate free space continuously decrease. At relatively short aging times, high supersaturation results in high nucleation current which leads to the formation of relatively finer Fe_2Ti precipitates with high number density. However, with increasing aging time,
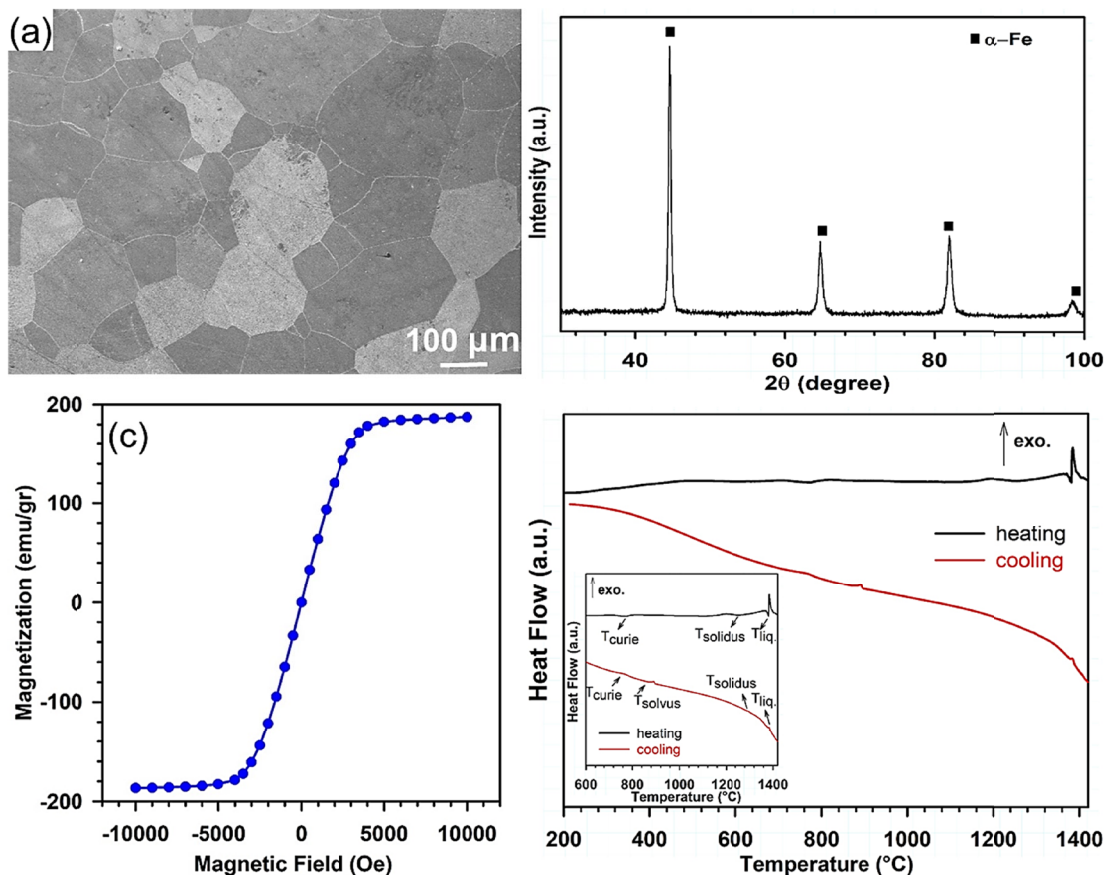

Fig. 1. (a) The SEM micrograph, (b) XRD pattern, (c) hysteresis curve and (d) DSC heating and cooling curves for the as-cast Fe-4Cr-6Ti alloy
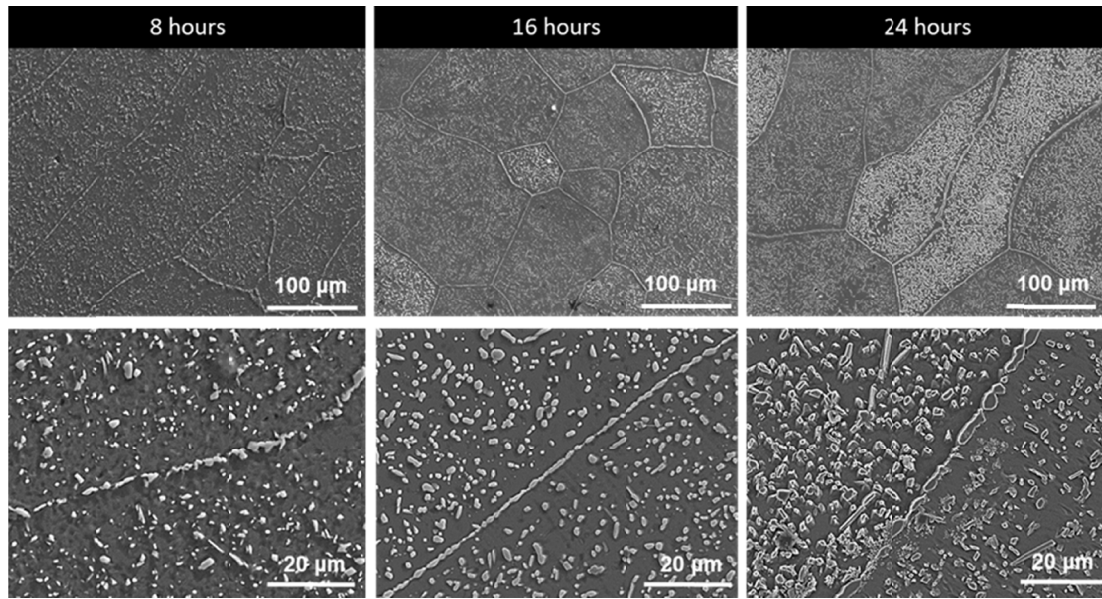
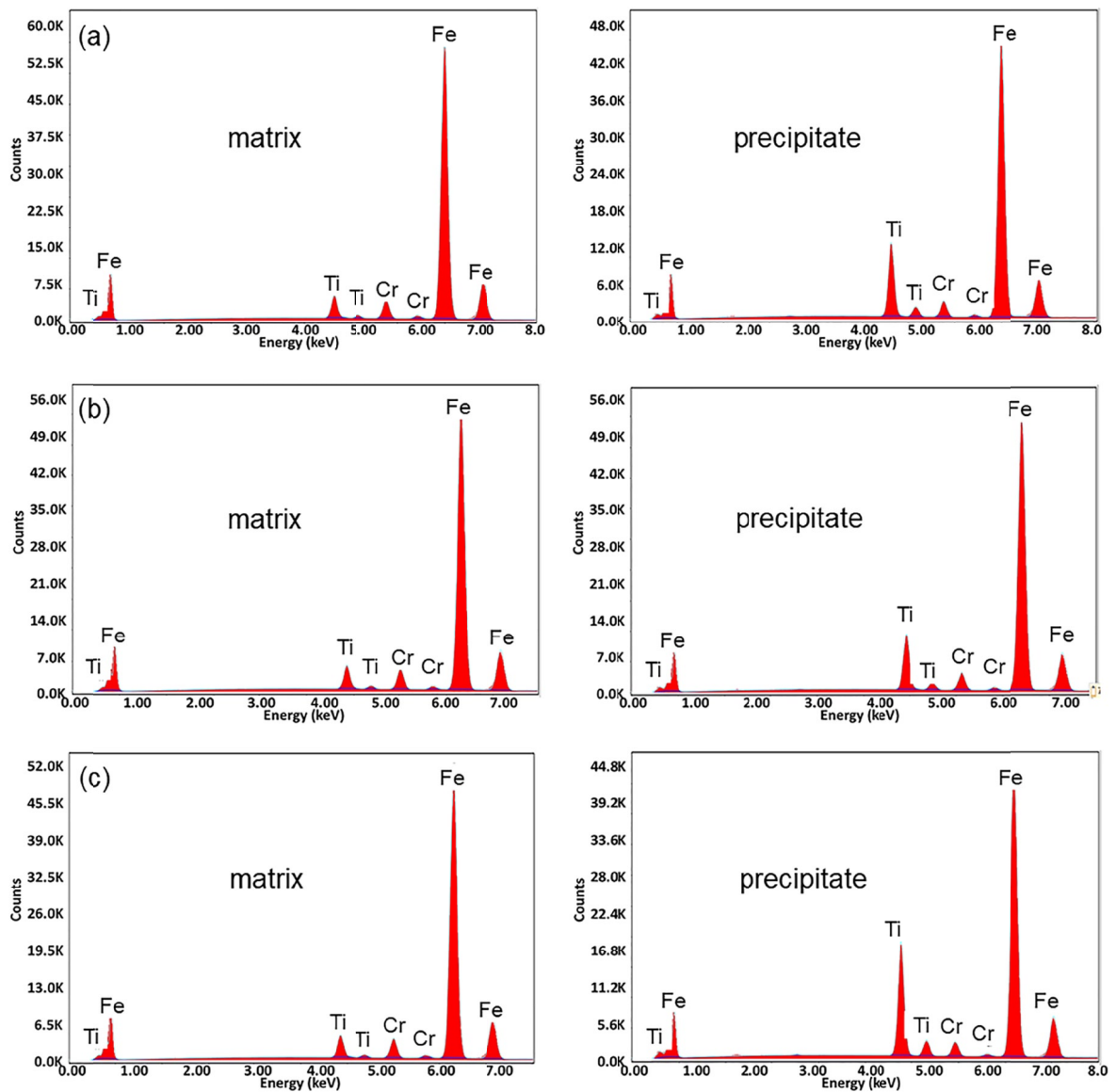Fig. 2. The SEM micrographs of the aged Fe-4Cr-6Ti samples

Fig. 3. The EDS analyses of the aged Fe-4Cr-6Ti samples; (a) 8 h, (b) 16 h, and (c) 24 h

the growth and coarsening of the Fe_2Ti precipitates is more rapid thereby relatively coarser precipitates and lower number density [30, 43-46]. In addition, the sizes of the grain boundary precipitates (TABLE 3) are considerably larger than those for grain interior. Contrary to the precipitates inside the grains, the highest precipitate size and the lowest fraction of grain boundary precipitates are observed for 8 h aging time. With increasing aging time, the fraction of grain boundary precipitates increases and their sizes decrease.

TABLE 3

Temporal development of the Fe_2Ti Laves phase in aged Fe-4Cr-6Ti samples

Aging time (h)	Precipitates inside the grains			Grain boundary precipitates	
	R (nm)	A_f (%)	N_V (m^{-3})	R (nm)	A_f (%)
8	544 ± 10	7.6	1,63*10^{20}	293 ± 15	82
16	664 ± 12	12.7	1,11*10^{20}	280 ± 09	91
24	810 ± 16	16.4	8,56*10^{19}	355 ± 13	90

* The circular equivalent radius (R), the areal fraction (A_f), and the number density (N_V) of the Fe_2Ti precipitates.

Moreover, the microstructural examinations also reveal that the precipitate free zones (PZF) are observed near the grain boundaries of α-Fe grains. The presence of the PZFs obviously implies that Fe_2Ti Laves phase particles nucleate first at grain boundaries and subsequently within the grains [47]. The formation of PZFs is generally attributed to two main reasons: (i) heterogeneous nucleation of the precipitates on vacancies. The amount of vacancies are extremely higher at the grain boundaries compared to grain interior. Thus, excess precipitates are present at the grain boundaries. (ii) The solute consumption near the grain boundaries leading to the depletion in supersaturation for formation of the precipitates [48,49].

The growth and the coarsening behavior of fine Fe_2Ti precipitates in aged samples is investigated by analyzing the precipitate size distributions (PSD). The PSDs for each aging condition are shown in Fig. 4. With increasing aging time, the PSDs do not broaden and the height maximum is not decreased which implies that the Fe_2Ti precipitates is not coarsened. This finding indicates that the microstructure of the aged Fe-4Cr-6Ti alloys have good thermal stability which is a very significant issue for structural applications at high temperatures [50,51].
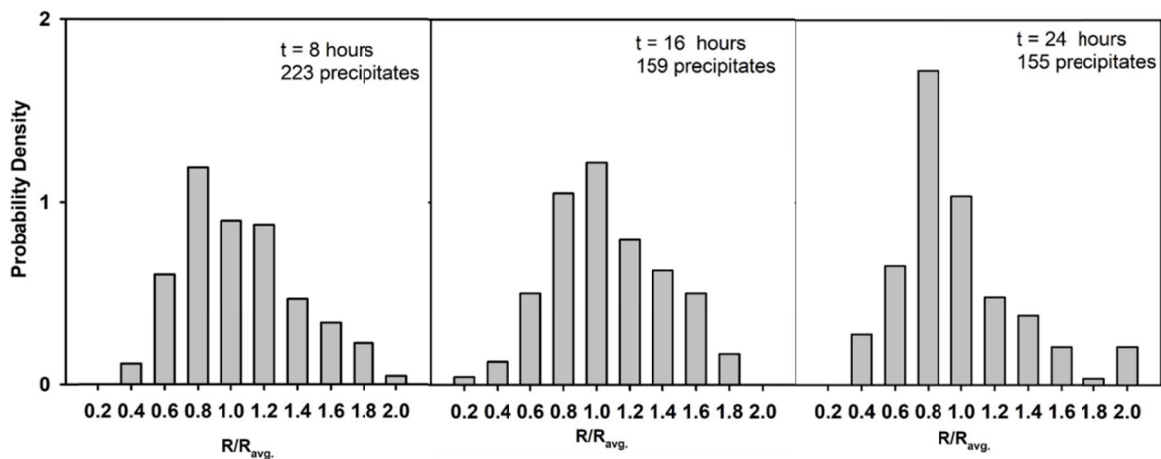

Fig. 4. Precipitate size distributions for aged Fe-4Cr-6Ti samples
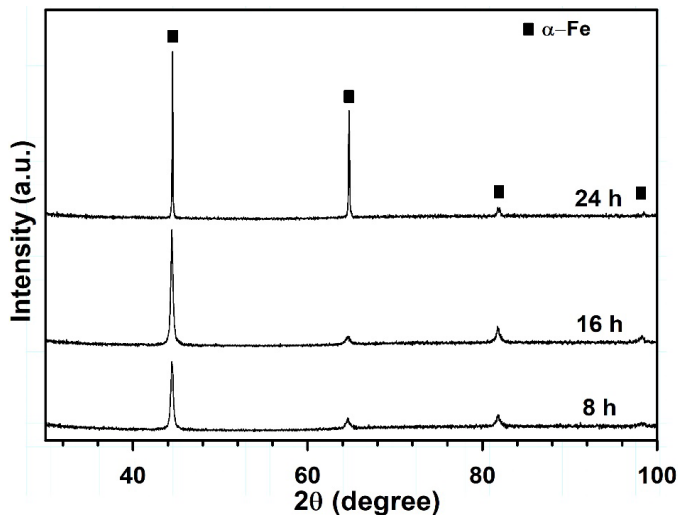

Fig. 5. The XRD patterns of the aged Fe-4Cr-6Ti samples

The XRD patterns of the aged Fe-4Cr-6Ti samples are given in Fig. 5. Although the SEM micrographs (Fig. 2) clearly show the precipitation of Fe_2Ti particles within the grains and along the grain boundaries, any diffraction peak corresponding to the Fe_2Ti Laves phase is not observed in the XRD analysis of the aged samples. This can be attributed to the fact that the volume fraction of the Fe_2Ti Laves phase is below the detection limit of the XRD analysis. Moreover, the lattice parameter of α-Fe phase for the aged Fe-4Cr-6Ti samples is also calculated. The calculated lattice parameters of the α-Fe phase are 2.882, 2.880 and 2.876 Å for the 8, 16 and 24 h aged samples, respectively. The decrease of the lattice parameter with increasing aging time is directly attributed to the microstructural features. With increasing aging time, the amount of fine Fe_2Ti precipitates noticeably increases leading to the depletion of Ti content of the supersaturated α-Fe solid solution. As the atomic radius

of Ti is significantly higher than that of Fe, the lattice parameter of α-Fe matrix phase decreases.

Although the formation of Fe$_2$Ti Laves phase is not observed by XRD analysis, the magnetic measurements (Fig. 6) of the aged samples confirm the presence of the Fe$_2$Ti precipitates. The hysteresis curves of the aged Fe-4Cr-6Ti samples reveal that all aged samples exhibit ferromagnetic behavior. The remarkable difference between the hysteresis curves of each sample is saturation magnetization M_s values. The M_s values of the aged Fe-4Cr-6Ti samples gradually decreases with increasing aging time. It is well-known that α-Fe phase is ferromagnetic, whereas Fe$_2$Ti Laves phase is paramagnetic at room temperature [52]. With increasing aging time, the volume fraction of paramagnetic Fe$_2$Ti Laves phase increases and the volume fraction of ferromagnetic α-Fe phase decreases. Thus, the M$_s$ values decreases from 180.3 to 163.3 emu/g. Compared to aged samples, the M_s value of the as-cast Fe-4Cr-6Ti sample (Fig. 1(c)) is relatively higher due to the supersaturated ferromagnetic α-Fe phase without noticeable formation of Fe$_2$Ti precipitates.
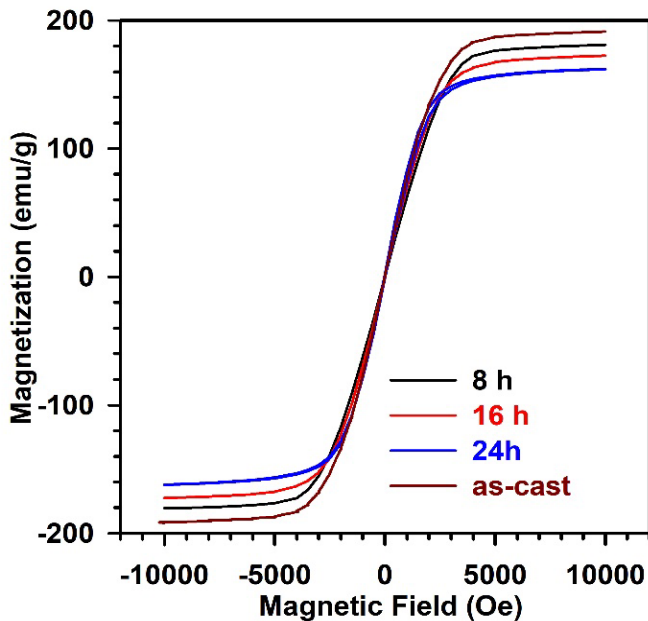

Fig. 6. The hysteresis curves of the aged Fe-4Cr-6Ti samples

The room-temperature mechanical properties of as-cast and aged Fe-4Cr-6Ti alloys are investigated by means of Vickers microhardness measurements (TABLE 4). Microhardness measurements implicitly display the dynamics of the precipitation sequence via hardness or strength alterations [30,45,46]. In addition, the microhardness value strongly depends on the size and amount of the precipitates. Compared to as-cast alloy, aged alloys exhibit relatively higher microhardness values. The higher microhardness values of aged samples are directly attributed to the formation of fine, hard and brittle Fe$_2$Ti Laves phase after isothermal aging. In addition, as the aging time increases, the microhardness values gradually increase. Although the size of the Fe$_2$Ti Laves phase precipitates considerably increase with increasing aging time, no decrease is observed for the microhard-

ness values. Thus, it is inferred that amount of the Fe$_2$Ti Laves phase is the dominant factor controlling the hardness of the Fe-4Cr-6Ti alloys isothermally aged at 800°C for 8, 16 and 24 h.

TABLE 4

Microhardness values (HV0.5) for as-cast and aged Fe-4Cr-6Ti samples

Sample	Vickers Microhardness (HV0.5)
As-cast	202.1
8 h aged	203.5
16 h aged	228.6
24 h aged	238.4

3.3. Cyclic Oxidation Behavior

Fig. 7(a) presents the net mass gain per specimen surface area versus number of cycles curve for 24 h aged Fe-4Cr-6Ti alloy isothermally oxidized at 500°C in atmospheric laboratory air. Net mass gain represents the oxidation products adherent to sample, spalled off oxides are excluded. Although the weight gain seems to have increasing tendency with time, important scale spallation is observed during the oxidation cycles. Typical parabolic rate equation is used in order to characterize the oxidation behavior of 24 h aged Fe-4Cr-6Ti sample.

$$\left(\frac{\Delta W}{A}\right)^2 = k_p t \tag{2}$$

where ΔW is the weight increment, A is the surface area, t is the oxidation time and k_p is the parabolic rate constant. The value of k_p is calculated from the slope of the linear regression-fitted $(\Delta W/A)^2$ vs. time plot (Fig. 7(b)). The value of the calculated rate constant is 2×10^{-6} mg^2/(cm^{4}s). Oxidation behavior of alloys at high temperature is a complex issue. The oxidation kinetics is influenced by several internal and external factors including temperature, atmosphere, composition of the oxidation products, and presence of cracks, etc. Therefore, oxidation kinetics may not follow parabolic rate law well [53].

In such conditions, it is more proper to use the instantaneous parabolic rate constant (k_i) in order to study the high temperature oxidation kinetics of alloys and intermetallic compounds [54-56]. The value of the instantaneous parabolic rate constant (k_i) can be calculated by fitting the $(\Delta W/A)^2$ vs. time plot by a fourth-order polynomial curve

$$\left(\frac{\Delta W}{A}\right)^2 = a_1 + a_2 t + a_3 t^2 + a_4 t^3 + a_5 t^4 \tag{3}$$

where a_1, a_2, a_3, a_4 and a_5 are regression-fitted constants. The k_i at any time (Fig. 7(c)) can be found from the differentiation of Eq. (2). It is clear that k_i for 24 h aged Fe-4Cr-6Ti sample is time dependent, first decreases, and then slightly increases with time. The variation of the k_i value with time indicates that scale
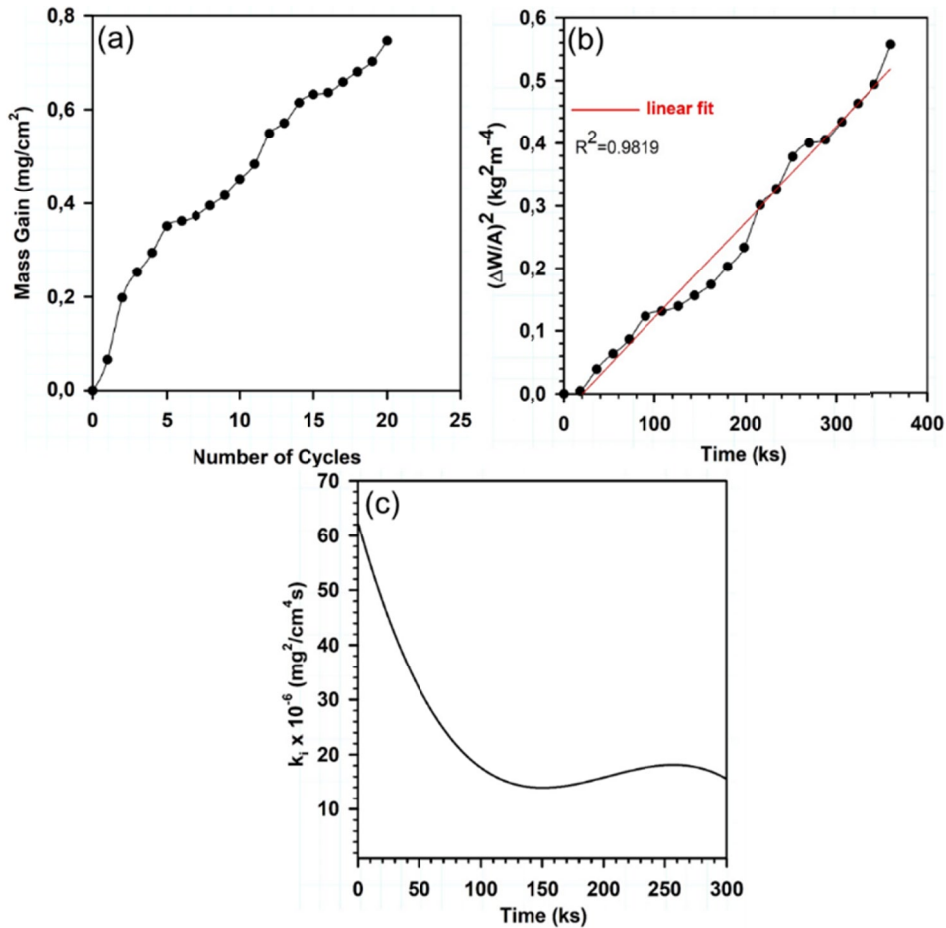
Fig. 7. (a) Mass gain per surface area versus oxidation time plot, (b) parabolic rate law plots and (c) instantaneous parabolic rate constant plots for the 24 h aged Fe-4Cr-6Ti sample oxidized at 500°C

characteristics and/or diffusion mechanisms are changed during oxidation [53,56]. Structure, chemical composition, uniformity, adherence and presence of cracks or porosity are the important parameters that strongly affect the oxidation behavior. In our
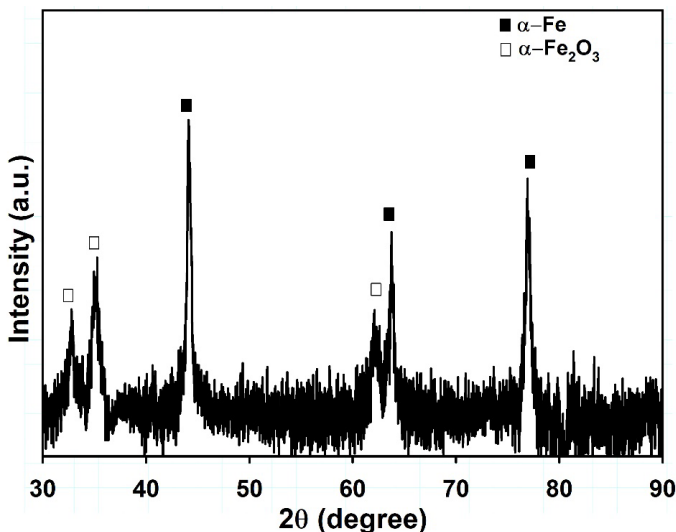

Fig. 8. XRD pattern for the 24 h aged Fe-4Cr-6Ti sample oxidized at 500°C

case, weak adherence of oxidation product and important scale spallation cause a considerable variations in the oxidation rate.

The oxidation product is identified as α-Fe_2O_3 (hematite, JCPDS No: 33-0664) by XRD analysis (Fig. 8). Any other oxide peaks are not detected in the diffraction patterns. In addition to Fe_2O_3 peaks, weak intensity peaks of α-Fe are also detected. The reason for the presence of substrate peaks is strong spallation due to the weak adherence of Fe_2O_3 to the substrate.

Figure 9(a-c) illustrates the surface scale morphology of the 24 h aged Fe-4Cr-6Ti sample oxidized at 500°C. The surface of the oxidized sample is composed of two different regions: dark and light regions. Dark regions (Fig. 9(b)) are covered by adherent oxide scales which is not spalled. The scale has platelet-like morphology with uniform size and distribution. This scale is also identified as Fe_2O_3 with EDS analysis (Fig. 9(d)). On the other hand, light regions (Fig. 9(c)) are the spalled oxide layers seen as small isolated voids. The rough spalled regions indicate that spallation mostly occurred during cooling [56]. The EDS analysis of these regions (Fig. 9(e)) reveals the similar composition with that obtained for the substrate.

During cyclic oxidation, scale spallation is frequently occurred and should be taken into account. Oxide scales having poor adherence to the metallic substrate can be easily spalled
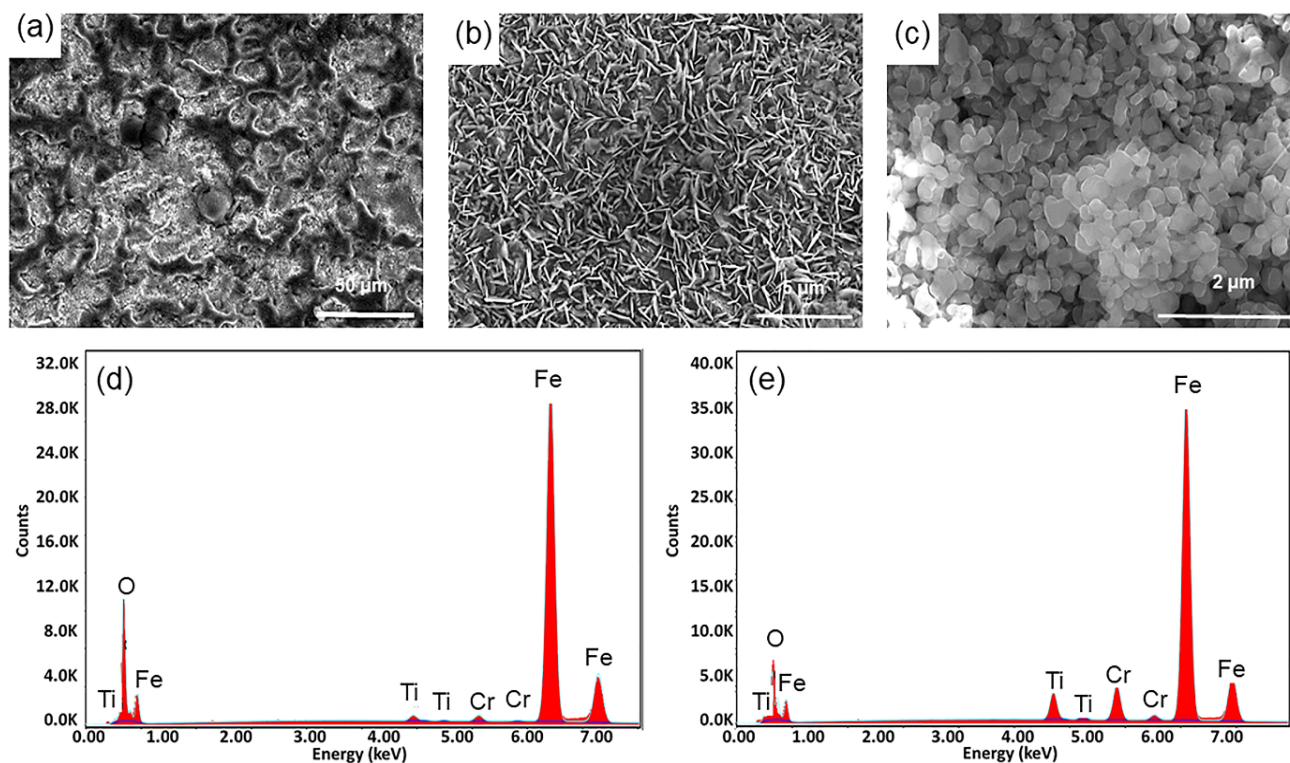
Fig. 9. SEM micrographs and EDS analysis of 24 h aged Fe-4Cr-6Ti sample isothermally oxidized at 500°C, (a) morphology of the surface, (b) adherent oxide scale (dark regions), (c) spallation region (light zones), (d) composition of the oxide scale and (e) composition of the spalled regions

off from the surface leading to an increase in the oxidation rate [57]. Thermal expansion mismatch between oxide and metallic substrate, scale thickness and temperature difference are the main factors that strongly affect the scale spallation resistance [58,59]. Among these factors, thermal expansion mismatch may be the most important factor. If the thermal expansion mismatch between the oxide scale and metallic substrate is high, compressive stresses are formed particularly during cooling. Thus, oxide scale cannot resist compressive stresses and spallation occurs [60-62]. Quadakkers et al. [62] reported that the thermal expansion mismatch between hematite (α-Fe_2O_3) and ferritic steel is larger compared to the mismatch between magnetite (Fe_3O_4) and ferritic steel. Therefore, they observed scale spallation in the outer layer due to the generation of compressive stresses during cooling.

The oxidation and scale spallation resistance of our model Fe-4Cr-6Ti alloy must be improved. In this respect, formation of protective and adherent oxide scales such as Cr_2O_3 will increase the oxidation and scale spallation resistance importantly. It is believed that the formation of non-protective Fe_2O_3 oxide should be hindered with increasing the Cr content of the alloy. Additionally, it is also believed that not only oxidation resistance but also the mechanical properties of the alloy may be increased with increasing the Ti content of the alloy. Mechanical properties will be improved due to the plentiful amount of Fe_2Ti Laves phase precipitates, whereas oxidation resistance will be increased with formation of TiO or TiO_2 scales which have better adherence than Fe_2O_3 scale [63].

4. Conclusions

The structural properties and oxidation behavior of a model ternary Fe-4Cr-6Ti ferritic alloy is examined in detail, and the important conclusions can be reported as follows:

i. The microstructure of the aged samples is composed of fine Fe_2Ti Laves phase precipitates and α-Fe (ferrite) matrix phase.

ii. With increasing aging time, the size and amount of the Fe_2Ti precipitates increased considerably leading to an important precipitation strengthening.

iii. 24 h aged specimen exhibited the highest precipitate radius, areal fraction and mean microhardness of value of 810 ± 16, 16.4% and 238.4 HV, respectively.

iv. The oxidation behavior of 24 h aged sample containing highest amount of precipitates reveals that α-Fe_2O_3 (hematite) is the only oxidation product.

v. The surface of the oxidized sample is rough due to the significant spallation of α-Fe_2O_3 scales.

REFERENCES

[1] S. Baik, M.J.S. Rawlings, D.C. Dunand, Effect of aging on coarsening- and creep resistance of a Ti-modified Fe-Ni-Al-Cr-Mo ferritic steel with L21/B2 composite precipitates, Materials Science and Engineering **A 776** 138987 (2020).

[2] D.G. Morris, I. Gutierrez-Urrutia, M.A. Muñoz-Morris, High temperature creep behaviour of an FeAl intermetallic strengthened by nanoscale oxide particles, International Journal of Plasticity **24** (7), 1205-1223 (2008).

[3] B. Hkdh, Design of ferritic creep-resistant steels, ISIJ international **41** (6), 626-640 (2001).

[4] C. Stallybrass, G. Sauthoff, Ferritic Fe-Al-Ni-Cr alloys with coherent precipitates for high-temperature applications, Materials Science and Engineering **A 387** 985-990 (2004).

[5] C. Stallybrass, A. Schneider, G. Sauthoff, The strengthening effect of (Ni,Fe)Al precipitates on the mechanical properties at high temperatures of ferritic Fe-Al-Ni-Cr alloys, Intermetallics **13** (12), 1263-1268 (2005).

[6] F. Masuyama, N. Komai, Creep Failure Behavior of Creep-Strength Enhanced Ferritic Steels ASME/JSME 2004 Pressure Vessels and Piping Conference, American Society of Mechanical Engineers Digital Collection, 107-114 (2004).

[7] X.P. Wang, A.M. Zhao, Z.Z. Zhao, Y. Huang, Y. Yu, Precipitation strengthening by nanometer-sized carbides in hot-rolled ferritic steels, Journal of Iron and Steel Research International **21** (12), 1140-1146 (2014).

[8] J. Chen, H. Liu, Z. Pan, K. Shi, H. Zhang, J. Li, Carbide evolution and service life of simulated post weld heat treated 2.25 Cr-1Mo steel, Materials Science and Engineering **A 622**, 153-159 (2015).

[9] V. Knežević, J. Balun, G. Sauthoff, G. Inden, A. Schneider, Design of martensitic/ferritic heat-resistant steels for application at 650°C with supporting thermodynamic modelling, Materials Science and Engineering **A 477** (1-2), 334-343 (2008).

[10] K. Sakuraya, H. Okada, F. Abe, BN type inclusions formed in high Cr ferritic heat resistant steel, Energy Materials **1** (3), 158-166 (2006).

[11] X. Zhou, C. Liu, L. Yu, Y. Liu, H. Li, Phase transformation behavior and microstructural control of high-Cr martensitic/ferritic heat-resistant steels for power and nuclear plants: a review, Journal of Materials Science & Technology **31** (3), 235-242 (2015).

[12] T. Horiuchi, M. Igarashi, F. Abe, Improved utilization of added B in 9Cr heat-resistant steels containing, W ISIJ International **42** (Suppl), S67-S71 (2002).

[13] V.G. Harris, D.J. Fatemi, K.B. Hathaway, Q. Huang, A. Mohan, G.J. Long, Atomic structure and magnetism of ordered and disordered Al0.5Fe0.5-xMnx alloys, Journal of Applied Physics **85** (8), 5181-5183 (1999).

[14] N. Takata, H. Ghassemi-Armaki, M. Takeyama, S. Kumar, Nanoindentation study on solid solution softening of Fe-rich Fe2Nb Laves phase by Ni in Fe-Nb-Ni ternary alloys, Intermetallics **70**, 7-16 (2016).

[15] K. Yamamoto, Y. Kimura, F.G. Wei, Y. Mishima, Design of Laves phase strengthened ferritic heat resisting steels in the Fe-Cr-Nb (–Ni) system, Materials Science and Engineering **A 329**, 249-254 (2002).

[16] M. Takeyama, N. Gomi, S. Morita, T. Matsuo, Phase Equilibria and Lattice Parameters of Fe 2 Nb Laves Phase in Fe-Ni-Nb Ternary System at Elevated Temperatures MRS Online Proceedings Library Archive 842 (2004).

[17] I. Tarigan, K. Kurata, N. Takata, T. Matsuo, M. Takeyama, Novel concept of creep strengthening mechanism using grain boundary Fe 2 Nb Laves phase in austenitic heat resistant steel MRS Online Proceedings Library Archive 1295 (2011).

[18] L. Machon, G. Sauthoff, Deformation behaviour of Al-containing C14 Laves phase alloys, Intermetallics **4** (6), 469-481 (1996).

[19] K. Yamamoto, Y. Kimura, Y. Mishima, Effect of matrix substructures on precipitation of the Laves phase in Fe-Cr-Nb-Ni system, ISIJ international **43** (8), 1253-1259 (2003).

[20] F. Abe, Effect of fine precipitation and subsequent coarsening of Fe 2 W Laves phase on the creep deformation behavior of tempered martensitic 9Cr-W steels, Metallurgical and Materials Transactions **A 36** (2), 321-332 (2005).

[21] E.Y. Plotnikov, Z. Mao, S. Baik, M. Yildirim, Y. Li, D. Cecchetti, R.D. Noebe, G. Martin, D.N. Seidman, A correlative four-dimensional study of phase-separation at the subnanoscale to nanoscale of a NiAl alloy, Acta materialia **171**, 306-333 (2019).

[22] G. Wang, H. Ding, R. Chen, J. Guo, H. Fu, Effect of current intensity on microstructure of Ni3Al intermetallics prepared by directional solidification electromagnetic cold crucible technique, Acta Metall. Sin. **53** (11), 1461-1468 (2017).

[23] J. Wu, C. Li, Y.C. Liu, Y. Wu, Q. Guo, H. Li, H. Wang, Effect of annealing treatment on microstructure evolution and creep behavior of a multiphase Ni3Al-based superalloy, Materials Science and Engineering **A 743**, 623-635 (2019).

[24] H. Chilukuru, K. Durst, S. Wadekar, M. Schwienheer, A. Scholz, C. Berger, K.H. Mayer, W. Blum, Coarsening of precipitates and degradation of creep resistance in tempered martensite steels, Materials Science and Engineering **A 510**, 81-87 (2009).

[25] T. Liu, C. Wang, H. Shen, W. Chou, N.Y. Iwata, A. Kimura, The effects of Cr and Al concentrations on the oxidation behavior of oxide dispersion strengthened ferritic alloys, Corrosion Science **76**, 310-316 (2013).

[26] T. Kaito, T. Narita, S. Ukai, Y. Matsuda, High temperature oxidation behavior of ODS steels, Journal of Nuclear Materials **329**, 333, 1388-1392 (2004).

[27] M.K. Miller, C.M. Parish, Q. Li, Advanced oxide dispersion strengthened and nanostructured ferritic alloys, Materials Science and Technology **29** (10), 1174-1178 (2013).

[28] K. Kawasaki, Y. Enomoto, Statistical theory of Ostwald ripening with elastic field interaction, Physica A: Statistical Mechanics and its Applications **150** (3), 463-498 (1988).

[29] K.E. Yoon, R.D. Noebe, D.N. Seidman, Effects of rhenium addition on the temporal evolution of the nanostructure and chemistry of a model Ni-Cr-Al superalloy. II: Analysis of the coarsening behavior, Acta Materialia **55** (4), 1159-1169 (2007).

[30] C.K. Sudbrack, T.D. Ziebell, R.D. Noebe, D.N. Seidman, Effects of a tungsten addition on the morphological evolution, spatial correlations and temporal evolution of a model Ni-Al-Cr superalloy, Acta Materialia **56** (3), 448-463 (2008).

[31] J.C. Russ, R.T. Dehoff, Springer Science & Business Media2012.

[32] I. Tarigan, N. Takata, M. Takeyama, Grain boundary precipitation strengthening mechanism by Fe2Nb Laves phase in creep of Fe-20Cr-30Ni-2Nb austenitic heat resistant steel, Proceedings of the 12th International Conference on Creep and Fracture of Engineering Materials and Structure (JIMIS 11), 2012.

[33] A.L. Sutton, W. Hume-Rothery, CXLI. The lattice spacings of solid solutions of titanium, vanadium, chromium, manganese, cobalt and nickel in α-iron The London, Edinburgh, and Dublin Philosophical Magazine and Journal of Science **46** (383), 1295-1309 (1955).

[34] E.P. Abrahamson, S.L. Lopata, The Lattice Parameters And Solubility Limits Of Alpha Iron As Affected By Some Binary Transition-Element Additions, Army Materials Research Agency Watertown Mass, 1966.

[35] R. Eris, M.V. Akdeniz, A.O. Mekhrabov, Atomic size effect of alloying elements on the formation, evolution and strengthening of γ'-Ni3Al precipitates in Ni-based superalloys, Intermetallics **109**, 37-47 (2019).

[36] G. Frommeyer, U. Brux, Microstructures and Mechanical Properties of High-Strength Fe-Mn-Al-C Light-Weight TRIPLEX Steels, Steel Research International **77** (9-10), 627-633 (2006).

[37] J.I. Schwerdt, G.F. Goya, M. Pilar Calatayud, C.B. Herenu, P.C. Reggiani, G.R. G., Magnetic field-assisted gene delivery: achievements and therapeutic potential, Current Gene Therapy **12** (2), 116-126 (2012).

[38] J.L. Murray, Phase diagrams of binary titanium alloys, ASM International 340-345 (1987).

[39] K.C.H. Kumar, P. Wollaiits, L. Delaey, Thermodynamic reassessment and calculation of Fe-Ti phase diagram, Calphad **18** (2), 223-234 (1994).

[40] L.F.S. Dumitrescu, M. Hillert, N. Sounders, Comparison of Fe-Ti Assessments, Journal of Phase Equilibria **19** (5), 441 (1998).

[41] G. Cacciamani, J. De Keyzer, R. Ferro, U.E. Klotz, J. Lacaze, P. Wollants, Critical evaluation of the Fe-Ni, Fe-Ti and Fe-Ni-Ti alloy systems, Intermetallics **14** (10-11), 1312-1325 (2006).

[42] L.I. Duarte, U.E. Klotz, C. Leinenbach, M. Palm, F. Stein, J.F. Löffler, Experimental study of the Fe-Ni-Ti system, Intermetallics **18** (3), 374-384 (2010).

[43] H.I. Aaronson, F.K. Legoues, Assessment of studies on homogeneous diffusional nucleation kinetics in binary metallic alloys, Metallurgical transactions, A, Physical Metallurgy And Materials Science **23 A** (7), 1915-1945 (1992).

[44] G. Martin, Solid state phase transformation in metals and alloys Orsay: Les Editions de Physique (1978).

[45] M.S. Atas, M. Yildirim, Temporal evolution, coarsening behavior and oxidation resistance of Ni-15Al superalloy, Journal of Alloys and Compounds **809**, 151784 (2019).

[46] M.S. Atas, M. Yildirim, Morphological Development, Coarsening, and Oxidation Behavior of Ni-Al-Nb Superalloys, Journal of Materials Engineering and Performance **29**, 4421-4434 (2020).

[47] M. Eumann, M. Palm, G. Sauthoff, Alloys based on Fe$_3$Al or FeAl with strengthening Mo$_3$Al precipitates, Intermetallics **12** (6), 625-633 (2004).

[48] P.N.T. Unwin, G.W. Lorimer, R.B. Nicholson, The origin of the grain boundary precipitate free zone, Acta Metallurgica **17** (11), 1363-1377 (1969).

[49] N. Ryum, The influence of a precipitate-free zone on the mechanical properties of an Al-Mg-Zn alloy, Acta Metallurgica **16** (3), 327-332 (1968).

[50] M. Yildirim, M.V. Akdeniz, M.A. O., Microstructural Investigation and Phase Relationships of Fe-Al-Hf, Alloys Metallurgical and Materials Transactions A **45** (8), 3412-3421 (2014).

[51] S. Milenkovic, M. Palm, Microstructure and mechanical properties of directionally solidified Fe-Al-Nb eutectic, Intermetallics **16** (10), 1212-1218 (2008).

[52] N. Wang, Y. Liu, H. Zhang, X. Chen, Y. Li, Effect of Co, Cu, Nb, Ti, V on magnetostriction and mechanical properties of TbDyFe alloys, Intermetallics **100**, 188-192 (2018).

[53] N. Babu, R. Balasubramaniam, A. Ghosh, High-temperature oxidation of Fe3Al-based iron aluminides in oxygen, Corrosion Science **43** (12), 2239-2254 (2001).

[54] C.H. Xu, W. Gao, H. Gong, Oxidation behaviour of FeAl intermetallics.The effects of Y and/or Zr on isothermal oxidation kinetics, Intermetallics **8** (7), 769-779 (2000).

[55] N. Birks, G.H. Meier, F. Pettit, Cambridge University Press2006.

[56] C.H. Xu, W. Gao, S. Li, Oxidation behaviour of FeAl intermetallics-the effect of Y on the scale spallation resistance, Corrosion Science **43** (4), 671-688 (2001).

[57] D. Vojtěch, T. Popela, J. Kubásek, J. Maixner, P. Novák, Comparison of Nb-and Ta-effectiveness for improvement of the cyclic oxidation resistance of TiAl-based intermetallics, Intermetallics **19** (4), 493-501 (2011).

[58] D. Vojtěch, J. Čížkovský, P. Novák, J. Šerák, T. Fabián, Effect of niobium on the structure and high-temperature oxidation of TiAl-Ti5Si3 eutectic alloy, Intermetallics **16** (7), 896-903 (2008).

[59] H.J. Grabke, M. Schütze, John Wiley & Sons2008.

[60] M.A. Montealegre, J.L. González-Carrasco, M.A. Munoz-Morris, Oxidation behaviour of Fe40Al alloy strip, Intermetallics **9** (6), 487-492 (2001).

[61] P.F. Tortorelli, K. Natesan, Critical factors affecting the high-temperature corrosion performance of iron aluminides, Materials Science and Engineering **A 258** (1-2), 115-125 (1998).

[62] W.J. Quadakkers, P.J. Ennis, J. Zurek, M. Michalik, Steam oxidation of ferritic steels – laboratory test kinetic data, Materials at High Temperatures **22** (1-2), 47-60 (2005).

[63] L. Dingqiang, X. Yun, L. Dongliang, Oxidation behavior of FeAl alloys with and without titanium, Journal of Materials Science **36** (4), 979-983 (2001).